energies

MDPI

Article

Thermochemical Storage of Middle Temperature Wasted Heat by Functionalized C/$Mg(OH)_2$ Hybrid Materials

Emanuela Mastronardo [1,2,*], Yukitaka Kato [3], Lucio Bonaccorsi [4], Elpida Piperopoulos [2] and Candida Milone [2,*]

1 National Interuniversity Consortium of Materials Science and Technology (INSTM), 50121 Florence, Italy
2 Department of Engineering, University of Messina, 98166 Messina, Italy; epiperopoulos@unime.it
3 Laboratory for Advanced Nuclear Energy, Institute of Innovative Research, Tokyo Institute of Technology, Tokyo 152-8550, Japan; yukitaka@nr.titech.ac.jp
4 Department of Civil, Energetic, Environmental and Materials Engineering, Mediterranean University of Reggio Calabria, 89124 Reggio Calabria, Italy; lucio.bonaccorsi@unirc.it
* Correspondence: emastronardo@unime.it (E.M.); cmilone@unime.it (C.M.); Tel.: +39-090-397-7593 (E.M.); +39-090-397-7242 (C.M.)

Academic Editor: Francesco Calise
Received: 14 October 2016; Accepted: 29 December 2016; Published: 10 January 2017

Abstract: For the thermochemical performance implementation of $Mg(OH)_2$ as a heat storage medium, several hybrid materials have been investigated. For this study, high-performance hybrid materials have been developed by exploiting the authors' previous findings. Expanded graphite (EG)/carbon nanotubes (CNTs)-$Mg(OH)_2$ hybrid materials have been prepared through $Mg(OH)_2$ deposition-precipitation over functionalized, i.e., oxidized, or un-functionalized EG or CNTs. The heat storage performances of the carbon-based hybrid materials have been investigated through a laboratory-scale experimental simulation of the heat storage/release cycles, carried out by a thermogravimetric apparatus. This study offers a critical evaluation of the thermochemical performances of developed materials through their comparison in terms of heat storage and output capacities per mass and volume unit. It was demonstrated that both EG and CNTs improves the thermochemical performances of the storage medium in terms of reaction rate and conversion with respect to pure $Mg(OH)_2$. With functionalized EG/CNTs-$Mg(OH)_2$, (i) the potential heat storage and output capacities per mass unit of $Mg(OH)_2$ have been completely exploited; and (ii) higher heat storage and output capacities per volume unit were obtained. That means, for technological applications, as smaller volume at equal stored/released heat.

Keywords: thermochemical storage; magnesium hydroxide; exfoliated graphite; graphene oxide; carbon nanotubes

1. Introduction

About 20%–50% of the energy consumed by industrial processes is lost as waste heat contained in streams of hot exhaust gases and liquids, as well as through heat conduction, convection, and radiation from hot equipment surfaces and from heated product streams [1]. This waste heat is produced whenever the operation is running. The current restrictive global energetic policy, the conservation of fossil resources, CO_2 abatement, and cost savings are the driving forces for the development of more efficient processes [2].

Thermal energy storage (TES) systems comprise all of the technologies that store thermal energy by heating or cooling a storage medium so that the stored energy can be used at a later time [2,3]. Indeed, through TES technologies, industrial users can put wasted energy back into the process that

created it, route the power somewhere else in the facility, or sell it to the grid. Thus, reducing peak demand, energy consumption, CO_2 emissions and costs, while increasing overall efficiency of the processes. Since the energetic demand of industrial processes may vary during any given day and from one day to next, TES systems can help to balance energetic demand and supply on a daily, weekly and even seasonal basis.

There are three kinds of TES systems: (1) sensible heat storage, which is based on storing thermal energy by heating or cooling a liquid or solid storage medium (e.g., water, sand, molten salts, rocks) [4]; (2) latent heat storage through phase change materials—PCMs—(e.g., from a solid state into a liquid state) [5]; and (3) thermo-chemical storage (TCS), which uses reversible chemical reactions to store and release thermal energy on demand [6].

Currently, TES systems based on sensible heat are commercially available while TCS and PCM-based storage systems are mostly under development and demonstration. The commercial deployment of TCS and PCM technologies is dependent on challenges in energy density, power performance, lifetime, charging capabilities, and costs.

Sensible heat storage is relatively inexpensive compared to PCM and TCS technologies. However, it requires large volumes because of its low energy density (i.e., three and five times lower than that of PCM and TCS systems, respectively) [3]. TCS can offer even higher storage capacities [7] and is especially suitable for long-term energy storage (e.g., seasonal storage), considering that heat is stored until the reactants remain separate for an infinitely long time. This means that heat can be released when required by the user.

For the TCS technology, materials are the key issues. The choice of a TCS material must be defined on the base of several parameters [8]:

- cost,
- cycling behavior (reversibility and degradation over large numbers of cycles),
- availability,
- toxicity and safety,
- corrosiveness,
- energy storage density,
- reaction temperature, and
- reaction rate.

Several TCS materials have been selected and investigated [9] on the basis of the desired waste heat temperatures. For instance, carbonate systems (e.g., $PbCO_3/PbO$, $CaCO_3/CaO$) [10,11] and $Ca(OH)_2/CaO$ [12] can be used to store heat at 450 °C and above. Metallic hydrates (e.g., LiH/Li, CaH_2/Ca, MgH_2/Mg) [13] and redox systems (e.g., Co_3O_4/CoO, BaO_2/BaO) [14,15] have been studied for heat storage between 700 °C and 1100 °C.

This study focuses on the $Mg(OH)_2/MgO$ TCS system, for middle-temperature waste heat. Indeed, it operates in the temperature range 200–400 °C that is typical for exhaust gas of different processes (e.g., gas turbine exhaust, steam boiler exhaust, drying and baking ovens, reciprocating engine exhaust). The $Mg(OH)_2/MgO$ TCS system is based on the following reversible chemical reaction and is characterized by the following reaction enthalpy (ΔH^0) [16]:

$$Mg(OH)_2\ (s) \leftrightarrow MgO\ (s) + H_2O\ (g),\ \Delta H^0 = \pm 81\ kJ/mol \quad (1)$$

The endothermic $Mg(OH)_2$ dehydration reaction corresponds to the heat storage phase. The heat is released when required through the exothermic hydration. The water vapour produced during the dehydration reaction is condensed and stored in a water tank and then reused for the subsequent hydration reaction.

The $Mg(OH)_2/MgO$ system, according to the Gibbs' phase rule, is mono-variant. The reaction temperature (T) and the vapor partial pressure (P_{H_2O}/P_0) are correlated by a univocal correspondence through the integral Van't Hoff equation:

$$\ln\left(\frac{P_{H_2O}(T)}{P_0}\right) = -\frac{\Delta H^0(T)}{RT} + \frac{\Delta S^0(T)}{R} \quad (2)$$

where ΔS^0 is the reaction (1) entropy (equal to 152.4 kJ/mol·K) and R is the ideal gas constant (equal to 8.314 J/mol·K). At equilibrium conditions, the reaction temperature (T_{eq}) is calculated as follows:

$$T_{eq} = \frac{\Delta H^0(T_{eq})}{\Delta S^0(T_{eq})} = 531 \text{ K} \quad (3)$$

The dehydration reaction requires an extra heat supply, in addition to the reaction heat, to raise the sample's temperature to the dehydration point.

The performance implementation of this storage medium is still an object of study. In order to increase its heat transfer property and to avoid the coalescence of the MgO product, which leads to grain growth and loss of bulk porosity diminishing the MgO rehydration kinetics, several strategies have been investigated. With vermiculite was used for the confinement of $Mg(OH)_2$ in its pores [17] and to avoid the coalescence of the MgO product. With vermiculite, it was not possible to improve the heat transfer property of $Mg(OH)_2$ considering its well-known low thermal conductivity. Zamengo et al. [18] experimentally observed the benefits of using expanded graphite (EG) as a heat-transfer enhancer for the dehydration/hydration reaction of $Mg(OH)_2/MgO$ system. However, the composite exhibited contact instability between two components. For improving the interaction between the organic (EG) and inorganic phase ($Mg(OH)_2$), the authors used a synthetic strategy through a deposition-precipitation method [19]. The compatibility between the two components has been improved by the electrostatic interaction promoted by the different point of zero charge (pH_{PZC}) of the materials. This synthetic strategy has also been applied on carbon nanotubes (CNTs) [20], which have been chosen not only for their high thermal conductivity but also for acting as a $Mg(OH)_2$ confining matrix due to their porous structure. From this study [20], it was demonstrated that thanks to the presence of CNTs the maximum potential heat storage capacity of $Mg(OH)_2$ per mass unit (~1300 $kJ/_{kgMg(OH)_2}$) has been fully exploited. The introduction of oxygenated functionalities upon CNTs surface was fundamental to bettering the MgO hydration reaction kinetics [20].

A critical evaluation of the thermochemical performances of EG/CNTs-$Mg(OH)_2$ hybrid materials is proposed here. In this study, the synthetic approach by deposition-precipitation previously studied by the authors in [19,20] has been extended to another type of carbonaceous support: graphene oxide (GO). Carbonaceous materials have been used both as such and functionalized. In case of CNTs, functionalization, i.e., surface oxidation, has been carried out with HNO_3 vapours according to the procedure reported in literature [21]. Functionalized CNTs for briefness are named F-CNTs. While, in the case of EG, a stronger oxidation treatment has been used to obtaining GO: the Hummers method [22]. It is expected that the functionalization treatment over EG surface could improve the MgO hydration reaction kinetics as previously observed in case of F-CNTs.

The heat storage performances of the carbon-based hybrid materials have been investigated through an experimental simulation of the heat storage/release cycles. The comparison between the developed materials has been carried out in terms of heat storage and output capacities per mass and volume unit in order to understand (i) if the maximum potential heat storage capacity of $Mg(OH)_2$ could be exploited and (ii) the impact of the presence of the carbonaceous phase on the estimated volumetric energy density.

2. Materials and Methods

2.1. Carbonaceus Materials

Two carbon-type materials have been used for this study: exfoliated graphite (EG) and CNTs. EG has been supplied by TIMREX C-THERM 002 TIMCAL Ltd. (Bironico, Switzerland), while CNTs were prepared by catalytic chemical vapor deposition (CCVD) of iso-butane (i-C_4H_{10}) as the C source in the presence of Fe dispersed on an Al_2O_3 catalyst, then purified to eliminate the catalyst residue [23].

EG and CNTs have been applied to the hybrid materials synthesis as such and modified through the insertion of oxygenated functionalities on their surface. Specifically, EG was treated though the well-known Hummers' method [22] to obtain GO, while, CNTs were oxidized in nitric acid vapour (HNO_3) at T = 135 °C for 120 min, in agreement with the procedure reported in literature [21]. The sample was named F-CNTs. With respect to the previous study [20], an implemented functionalization apparatus permitted to gain higher HNO_3 concentration in the vapour phase thus resulting in a stronger oxidative effect. The extent of the effects of the two functionalization treatments has been evaluated through thermogravimetric (TG) and derivative thermogravimetric analysis (DTG) in inert atmosphere (Ar) in the temperature range between 100°C and 900 °C (20 °C/min). The results are shown in Figure A1 of Appendix A.1.

2.2. Carbon-Based Hybrid Materials Preparation and Characterization

For the preparation of the Carbon/$Mg(OH)_2$ hybrid materials a deposition-precipitation route has been employed [20]. In detail, a specified amount of carbonaceous material (EG, GO, CNTs, or F-CNTs) was sonicated for 30 min in 50 mL of $Mg(NO_3)_2$ (purchased by Sigma Aldrich, Saint Louis, USA, Assay: 99%) solution. Then, 150 mL of NH_4OH 1 M (purchased by Carlo Erba, Milan, Italy, Assay: 30 wt %) solution was gradually added (2.5 mL/min) under magnetic stirring through a peristaltic pump. The final solution (pH ≈ 11.5) was aged at ambient conditions for 24 h, after which it was vacuum filtered (0.22 μm) and the collected solid was washed with deionized water and dried in a vacuum oven at 50 °C for 16 h.

The Mg^{2+} ions concentration in solution was chosen on the basis of the desired $Mg(OH)_2$ deposited amount. The initial moles of Mg^{2+} in the solution are those that theoretically should be precipitated in case of complete precipitation according to the stoichiometric reaction:

$$Mg(NO_3)_2 + 2NH_4OH \rightarrow Mg(OH)_2 + 2NH_4NO_3 \quad (4)$$

The $Mg(OH)_2$ load (wt %) of the hybrid materials was fixed at ~30% accordingly to previous studies [20], having obtained with this amount the better dispersion of $Mg(OH)_2$ among the CNTs.

Pure $Mg(OH)_2$ was synthesized according to the precipitation reaction reported above.

The prepared samples are listed in Table 1, reporting the relative carbon type of which the hybrid materials are made of, the $Mg(OH)_2$ load (wt %) and the bulk (or apparent) density.

The as-prepared samples were analysed by means of scanning electron microscopy (SEM, Quanta 450, FEI, Hillsboro, OR, USA) and X-Ray Diffraction (XRD, Bruker D8 Advance, Bruker, Billerica, MA, USA) to determining their morphology and crystal structure. The SEM analysis were performed on Cr-metallized samples and operating with an accelerating voltage of 10 kV under high vacuum conditions (6.92×10^{-5} Pa). The XRD apparatus has a Bragg-Brentano θ–2θ configuration, with Cu Kα radiation (40 V, 40 mA). XRD patterns were collected in the range 10°–80° with a step of 0.1°/s.

Table 1. Prepared hybrid materials. Description of the type of carbon used, $Mg(OH)_2$ load ($W_{Mg(OH)_2}$ (wt %)), and bulk density (ϱ (kg/m^3)) of the samples. GM: expanded graphite and magnesium hydroxide; GOM: graphite oxide and magnesium hydroxide; NM: carbon nanotubes and magnesium hydroxide; FNM: functionalized carbon nanotubes and magnesium hydroxide; EG: expanded graphite; GO: graphene oxide; and CNT: carbon nanotube.

Sample Code	Carbon Type	$Mg(OH)_2$ Load ($W_{Mg(OH)_2}$ (wt %))	Density (ϱ (kg/m^3))
$Mg(OH)_2$	-	100	350
GM	EG	33.4	150
GOM	GO	34.7	423
NM	CNTs	35.5	207
FNM	F-CNTs	31.0	765

2.3. Experimental Simulation of a Heat Storage/Release Cycle

A heat storage/release cycle basically consists of the succession of a dehydration and a hydration reaction. It was experimentally simultated through a TG unit (STA 449 F3 Jupiter, Netzsch, Selb, Germany) coupled with an evaporation system for the water vapour supply. The TG apparatus is equipped with a special furnace suitable for analysis in water vapour atmosphere. A dehydration/hydration cycle representative of the chemical heat pump (CHP) was carried out on ~20 mg as follows: the sample was first dried at 110 °C in inert atmosphere (N_2 flow rate: 100 mL/min) for 60 min to remove the physically-adsorbed water. Then, the temperature was increased at a constant rate (10 °C/min) to the desired dehydration temperature (T_d =350 °C) and $Mg(OH)_2$ dehydration reaction proceeded over 120 min. After the complete dehydration reaction, the temperature was decreased at constant rate (−10 °C/min) to the hydration temperature (T_h = 125 °C). The water vapour necessary for the MgO hydration reaction was supplied by the evaporation unit at 2.22 g/h and mixed with 35 mL/min N_2 as carrier gas. After the hydration reaction proceeded over 120 min, the water vapour supply was stopped and the sample was kept at 110 °C for 10 min under a constant N_2 flow (100 mL/min) to physically remove the adsorbed water from the sample. This process was repeated for each cycle.

Numerical Evaluation of the Hybrid Materials' Performances

Congruent with previous studies [19,20], the performances of the samples have been expressed in terms of reacted fraction (β (%)), calculated by the Equation (5):

$$\beta\ (\%) = \left(1 - \frac{\Delta m_{real}}{\Delta m_{th}}\right) \times 100, \tag{5}$$

where Δm_{real} (%) is the instantaneous real mass change, and Δm_{th} (%) is the theoretical mass change due to the dehydration of 1 mol $Mg(OH)_2$ normalized to the total amount present in the sample, respectively expressed by Equations (4) and (5):

$$\Delta m_{real}\ (\%) = \frac{m_{in} - m_{inst}}{m_{in}} \times 100, \tag{6}$$

$$\Delta m_{th}\ (\%) = \left(\frac{M_{Mg(OH)_2} - M_{MgO}}{M_{Mg(OH)_2}} \times 100\right) \times \frac{W_{Mg(OH)_2}}{100}, \tag{7}$$

where m_{in} (g) and m_{inst}(g) are respectively the initial sample mass and the instantaneous mass during the TG analysis. $M_{Mg(OH)_2}$ (g/mol) and M_{MgO} (g/mol) are, respectively, the molecular weight of $Mg(OH)_2$ and MgO, and $W_{Mg(OH)_2}$ is the $Mg(OH)_2$ load. In the case of 100% weight of $Mg(OH)_2$ present in the sample $\Delta m_{th} = 30.89\%$.

The dehydration and hydration conversions ($\Delta\beta_{d/h}$ (%)) are respectively expressed by Equations (8) and (9):

$$\Delta\beta_d\ (\%) = \beta_d^i - \beta_d^f \quad (8)$$

$$\Delta\beta_h\ (\%) = \beta_h - \beta_d^f, \quad (9)$$

where β_d^i (%) and β_d^f (%) are, respectively, the reacted fraction at the beginning and at the end of the dehydration treatment. While β_h (%) is the final reacted fraction of MgO at the point of water supply termination.

The heat storage and output capacities per mass ($Q_{s/r}^M$ ($kJ/kg_{Mg(OH)_2}$)) and volume unit ($Q_{s/r}^V$ (MJ/m^3)) were calculated respectively by the following Equations (10) and (11):

$$Q_{s/r}^M\ (kJ/kg_{Mg(OH)_2}) = -\frac{\Delta H^0}{M_{Mg(OH)_2}} \times \Delta\beta_{d/h} \quad (10)$$

$$Q_{s/r}^V\ (MJ/m^3) = -\frac{\Delta H^0}{M_{Mg(OH)_2}} \times \Delta\beta_{d/h} \times \varrho_c \times \frac{W_{Mg(OH)_2}}{100} \quad (11)$$

where ΔH^0 (kJ/mol) is the enthalpy of reaction, and ϱ_c (kg/m^3) is the density of the sample.

3. Results

3.1. Samples' Morphological and Structural Characterizations

As reported in Table 1, the hybrid materials containing the F-CNTs (FNM sample: functionalized nanotubes and magnesium hydroxide) and GO (GOM sample: graphene oxide and magnesium hydroxide) are characterized by higher bulk density values than the ones made of EG (GM sample: graphite and magnesium hydroxide) and CNTs (NM sample: nanotubes and magnesium hydroxide), and pure $Mg(OH)_2$. Specifically, the bulk density of the materials ranks in the order: FNM > GOM > $Mg(OH)_2$ > NM > GM.

The morphological aspect of the as prepared samples is shown by SEM micrographs in Figure 1. Pure $Mg(OH)_2$ (Figure 1a) has a plate-like morphology typical of brucite [24] and the platelets naturally tend to agglomerate. Upon $Mg(OH)_2$ deposition-precipitation over non-oxidized EG and CNTs a scarce interaction between the two components can be observed (Figure 1b,c). Indeed, the deposition-precipitation of $Mg(OH)_2$ upon EG (GM sample) leads to a poor carbonaceous surface covering (Figure 1b). In the case of the NM sample, few $Mg(OH)_2$ clusters (Figure 1c white circles) are sparse among the CNT bundles (Figure 1c black arrow). Both in GM and NM samples it cannot be excluded that bulk $Mg(OH)_2$ precipitation occurs without carbon (EG/CNTs) interaction. The lower bulk density values of GM and NM samples could be clarified at the light of their morphology. Indeed, due to the scarce interaction between $Mg(OH)_2$ and the carbonaceous phase, and to the larger amount of carbon (ca. 65–70 wt %) with respect to $Mg(OH)_2$ (ca. 30%–35%), the main contribution to the bulk density of hybrid samples could be determined by the carbonaceous phase that is characterized by low bulk density values (respectively, 40 and 170 g/cm^3 for EG and CNTs).

A stronger interaction is observed between $Mg(OH)_2$ and oxidized carbonaceous materials: GO and F-CNTs. Specifically, in the case of the GOM sample, $Mg(OH)_2$ densely packs the GO phase (Figure 1d), and, in the FNM sample, $Mg(OH)_2$ particles are homogeneously dispersed among the F-CNTs (Figure 1e). The more packed morphology of these last samples is totally in agreement with their bulk density values.

For the sake of completeness, SEM analysis of the carbonaceous materials are reported in Figure A2 of Appendix A.2.

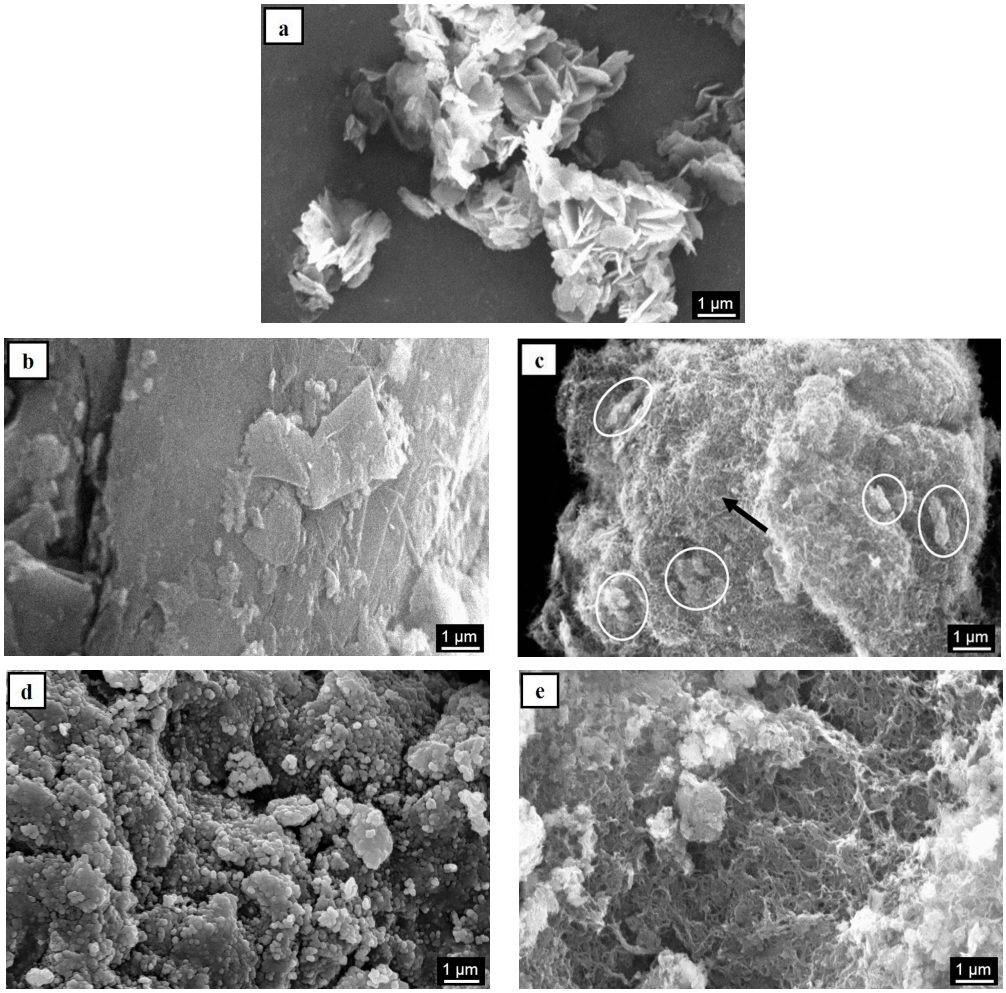

Figure 1. Scanning electron microscopy (SEM) micrographs of: (**a**) $Mg(OH)_2$; (**b**) GM; (**c**) NM; (**d**) GOM; and (**e**) FNM samples.

XRD analysis results are reported in Figure 2. As a common feature, the samples patterns show peaks relative to crystalline $Mg(OH)_2$ (2θ: 18.5°, 32.5°, 38°, 50.6°, 58.5°, 62°, 68°, 72°) and to the carbonaceous phase (2θ: 26.5°, 42.5°, 45°, 51°, 55°, 78°) in agreement with standard data (respectively JCPDS 7-0239 and JCPDS 25-0284), and no peaks arising from impurities. In the case of the GOM sample, it has to be pointed out that the most intense peak typical of GO at 2θ = 11.4° (shown in Figure A3 of Appendix A.3) has not been detected (see Figure 2c). The reason can be attributed in the preparation method of the hybrid material. Indeed, the $Mg(OH)_2$ deposition-precipitation over GO, as explained in the Materials and Methods section (Section 2), is driven by Equation (2), which gives as a by-product ammonium nitrate (NH_4NO_3) and residual ammonia (NH_4OH) being that the reaction is carried out with a large stoichiometric excess of the latter reagent. Ammonium hydroxide can be easily intercalated in the GO layers [25] and ammonium hydroxide acts as reducing agent [26]. It can be argued that the synergistic action of these two reagents leads to obtaining graphene, which explain why the GO diffraction peak cannot be detected, given that long-range order of the layer is too poor [27]. This is also in agreement with the small-angle XRD (1°–10°) pattern of the GOM sample (shown in Figure A3b of Appendix A.3), in which no peaks can be detected.

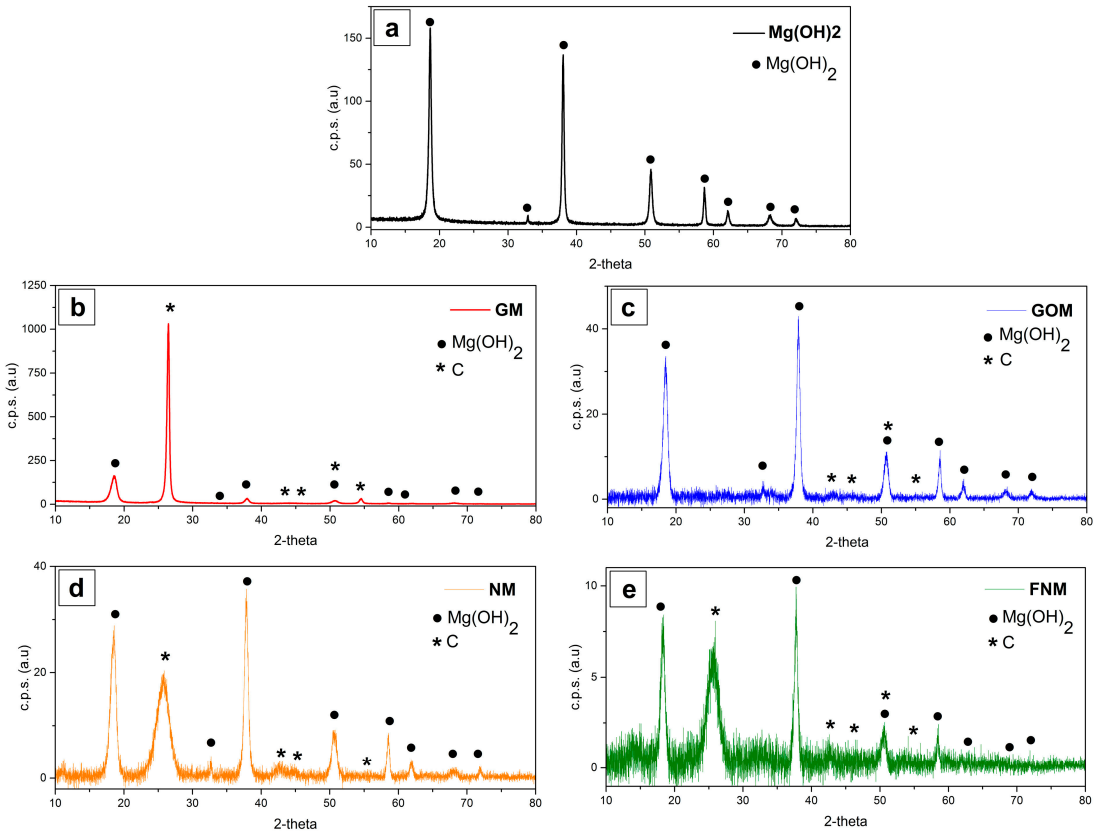

Figure 2. X-Ray Diffraction (XRD) analysis of (**a**) $Mg(OH)_2$; (**b**) GM; (**c**) GOM; (**d**) NM; and (**e**) FNM.

For a deeper comprehension of the $Mg(OH)_2$ crystal structure of the different hybrid materials, Figure 3 shows the comparison between the peaks relative only to the hydroxide phase. The $Mg(OH)_2$ intensity ratios of reflections [001] to [101] and [110] (I_{001}/I_{101}, I_{001}/I_{110}), which are labeled in Figure 3, are listed in Table 2.

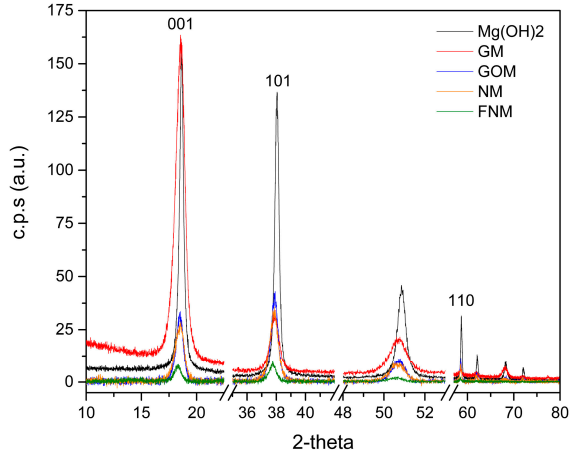

Figure 3. Comparison between all the samples of the peaks relative only to the $Mg(OH)_2$ phase.

In pure $Mg(OH)_2$, peaks are narrower and more intense than those of the hybrid materials. GOM and NM samples show similar features. The FNM sample is characterized by the broadest and less intense $Mg(OH)_2$ peaks, indicative of smaller particle sizes which is also in agreement with SEM analysis (Figure 1e).

Table 2. $Mg(OH)_2$ intensity ratios of reflections [001] to [101] and [110] (I_{001}/I_{101}, I_{001}/I_{110}).

Sample Code	I_{001}/I_{101}	I_{001}/I_{110}
$Mg(OH)_2$	1.1	5.7
GM	5.3	23.6
GOM	0.8	3.3
NM	0.8	3.3
FNM	0.9	4.4

$Mg(OH)_2$ particles, when pure, or combined with EG, are preferentially oriented to the (001) direction, while, in case of GOM, NM, and FNM samples, $Mg(OH)_2$ particles are preferentially oriented to the (101) direction.

3.2. Dehydration and Hydration Reactions

$Mg(OH)_2$ and hybrid materials have undergone three dehydration/hydration cycles experiments under conditions reported in Section 2.3.

Figure 4a,b shows the dehydration reaction curves, expressed in terms of reacted fraction (β (%)) as a function of reaction time (*t* (min)). The curves are relative to the third cycle, when the thermochemical behavior of the samples has been observed to be stable [19,20]. The reaction conversion rate (dβ/d*t* (%/min)) curves, relative to the first 60 min of the dehydration reaction, are shown in Figure 4c,d. Hydration curves are plotted in Figure 5a,b. The following reaction parameters are reported in Table 3: the temperatures of the derivative reacted fraction maximum peak (T_{peak} (°C)), the reaction conversion rate (dβ/d*t* (%/min)), and the dehydration/hydration conversions ($\Delta\beta_{d/h}$ (%)). The dehydration/hydration conversions are expressed considering a percentage error of 2% determined considering the measurement uncertainty derived from six repeated tests.

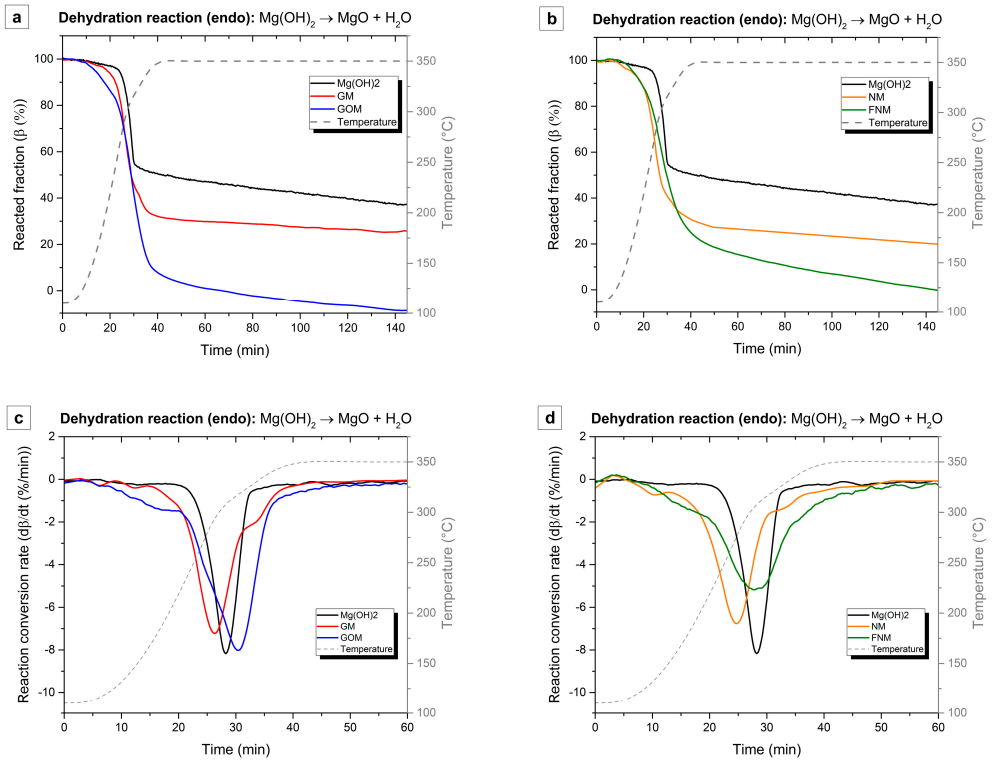

Figure 4. Dehydration reaction curves of (**a**) EG/GO and (**b**) CNTs/F-CNTs based hybrid materials; and the reaction conversion rate (dβ/d*t* (%/min)) curves of (**c**) EG/GO and (**d**) CNTs/F-CNTs-based hybrid materials.

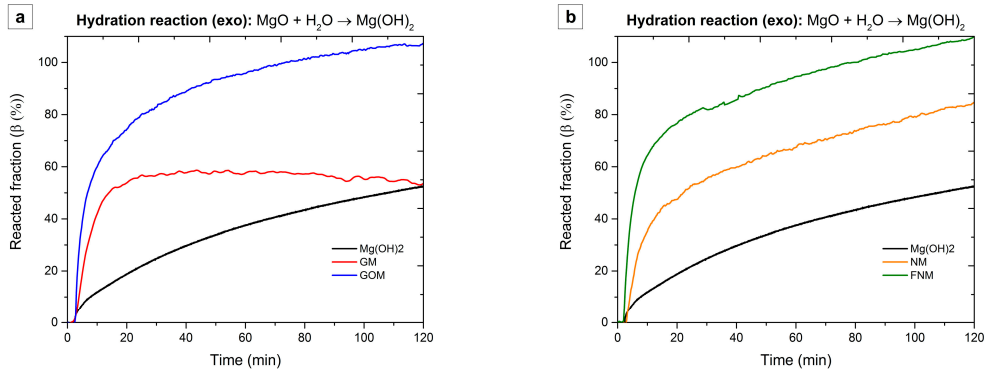

Figure 5. Hydration reaction curves of (**a**) EG/GO- and (**b**) CNTs/F-CNTs-based hybrid materials.

Table 3. Details of dehydration/hydration reactions: temperatures of the derivative reacted fraction maximum peak (T_{peak} (°C)), the reaction conversion rate (dβ/dt (%/min)), and the dehydration/hydration conversions ($\Delta\beta_{d/h}$ (%)).

Sample Code	T_{peak} (°C)	dβ/dt (%/min)	$\Delta\beta_d$ (%)	$\Delta\beta_h$ (%)
$Mg(OH)_2$	307	8.2 ± 0.2	62.1 ± 1.2	52.0 ± 1.0
GM	292	7.2 ± 0.1	74.2 ± 1.5	58.1 ± 1.2
GOM	318	8.0 ± 0.2	108.1 ± 2.2	106.0 ± 2.1
NM	282	6.7 ± 0.1	80.0 ± 1.6	83.2 ± 1.7
FNM	307	5.2 ± 0.1	100.3 ± 2.0	108.1 ± 2.2

From the dehydration profiles it is evident that, in the case of pure $Mg(OH)_2$, GM and NM samples show a single decomposition step occurring between 200 °C and 350 °C (Figure 4a,b) that can be clearly addressed to the $Mg(OH)_2$ dehydration reaction. GOM and FNM samples present a change in the curve slope which allows two overlapped dehydration processes to take place according to different reaction rates (Figure 4a,b). The fastest, which occurs between 200 °C and 350 °C, is clearly addressed to the $Mg(OH)_2$ dehydration reaction (as already seen for $Mg(OH)_2$, GM, and NM samples). The slowest, which occurs at lower temperatures (110–200 °C), can presumably be indicative of the structural water removal which can be retained by the hydrophilic oxygenated groups present on the carbonaceous surface [20]. For the sake of completeness, the TG profiles of GO and F-CNTs from 100 °C up to 1000 °C in an inert ambient environment (Ar 100 mL/min) are reported in Figure A1 of Appendix A.1. They show that upon heating up to 350 °C to drive the $Mg(OH)_2$ dehydration, oxygenated groups present on GO and F-CNTs surfaces are only partially decomposed. The remaining groups are able to physically retain the adsorbed water, thus explaining the first dehydration step.

The T_{peak} of pure $Mg(OH)_2$ and FNM sample is 307 °C (Figure 4d). This moves to lower values in the case of GM and NM samples, respectively, 292 °C and 282 °C (Figure 4c,d); while, in the case of the GOM sample, it is shifted towards a higher value: 318 °C (Figure 4c). The dehydration rate ranks in the order: $Mg(OH)_2 \approx$ GOM > GM > NM > FNM (the exact values are listed in Table 3).

The hydration reaction proceeds faster for hybrid materials than pure $Mg(OH)_2$, in particular for GOM and FNM samples (see Figure 5a,b). The hydration rate ranks in the order: GOM ≈ FNM > GM > NM > $Mg(OH)_2$.

Pure $Mg(OH)_2$ exhibits the lowest reaction conversion (Figure 6). Hybrid materials show even higher hydration conversion than pure $Mg(OH)_2$. The highest $\Delta\beta_{d/h}$ values are achieved for GOM and FNM samples. In this case reaction conversions slightly exceed the 100% value due to the contribution of the water physisorbed on the functionalized carbonaceous surface. The presence of physisorbed water has been previously observed in the dehydration curves plotted in Figure 4a,b.

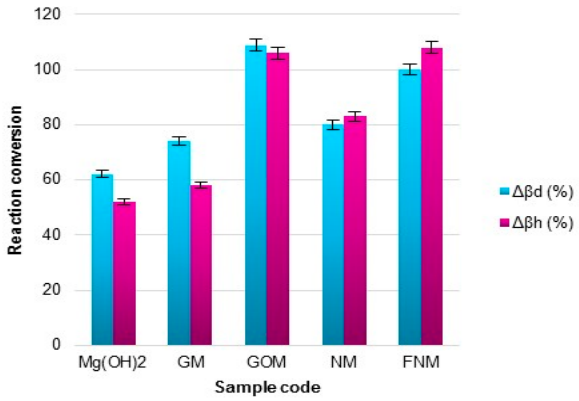

Figure 6. Dehydration and hydration reaction conversions ($\Delta\beta_{d/h}$ (%)).

3.3. Heat Storage and Output Capacities

Stored/released heat per mass unit ($Q^M_{s/r}$) curves (Figure 7a,b) give an indication about how much of the $Mg(OH)_2$ potential heat storage and output capacities have been exploited. The theoretical maximum heat storage capacity of pure $Mg(OH)_2$ can be easily calculated from the dehydration reaction enthalpy change ($\Delta H^0 = \pm 81$ kJ/mol) and its molecular weight ($M_{Mg(OH)_2} = 58.3$ g/mol). The value is 1389 $kJ/kg_{Mg(OH)_2}$.

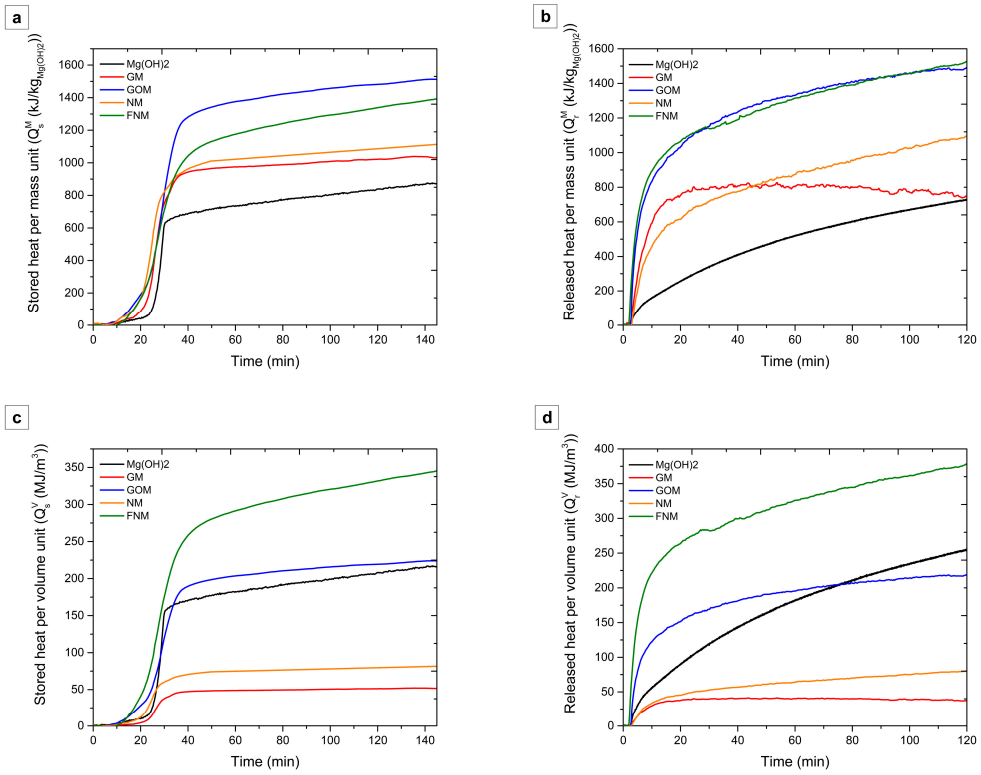

Figure 7. (**a**) Stored and (**b**) released heat per mass unit; (**c**) stored and (**d**) released heat per volume unit.

As it can be observed from the curves of the stored and released heat per mass unit (Figure 7c,d), congruent to previous studies [20] with pure $Mg(OH)_2$, only half of its capacity is used. Hybrid materials show higher stored and released heat per mass unit than $Mg(OH)_2$, with GOM and FNM samples fully exploiting $Mg(OH)_2$ heat storage/output capacity.

The stored/released heat per volume unit capacity ($Q^V_{s/r}$), i.e., the volumetric energy density, is a benchmark for comparing the different storage materials. This gives an indication of the global efficiency of the hybrid material. Indeed, despite its fundamental role in enhancing the performances of the storage medium, the carbonaceous phase could be intended as an "inert" component since it does not directly participate to the dehydration/reaction.

The stored/released heat per volume unit curves are plotted in Figure 7c,d.

The stored/released heat capacity per volume unit (i.e., volumetric energy density) of a material, as can be derived from its expression in Equation (11), directly depends from the bulk material density and its dehydration/hydration conversion. Hence, at equal $Mg(OH)_2$ content the higher these two parameters are, the higher the volumetric energy density. In case of hybrid materials, it also depends from the $Mg(OH)_2$ load: the lower the content, the lower the volumetric energy density. Due to its high density and dehydration/hydration conversion, the FNM sample exhibits the highest volumetric energy density, ~340 MJ/m^3. Pure $Mg(OH)_2$ volume energy density is comparable to that of the GOM sample (~220 MJ/m^3). NM and GM samples exhibit the lowest volumetric energy density, respectively, at ~80 and ~52 MJ/m^3.

4. Discussion

Despite pure $Mg(OH)_2$ exhibiting the highest dehydration reaction rate (Figure 4), it shows the lowest reaction conversion and the worst rehydration kinetics, in terms of reaction rate.

Demonstrating that, in agreement with previous studies [19,20], the carbonaceous phase is fundamental in order to improve the thermochemical performances of storage medium in terms of reaction conversion and kinetics, it was evaluated with this study if and how the functionalization treatment influences the thermochemical performances of either CNT- and EG-based hybrid materials.

Both functionalized CNTs and EG allowed obtaining the highest reaction conversion and the fastest rehydration, which means that through FNM and GOM, in the case of their application as heat storage materials, it is possible to fully exploit the $Mg(OH)_2$ potential heat storage capacity, and that they can deliver to the user almost immediately (~10 min) all of the stored heat in the case of energetic demand, as evinced from Figure 7b,d.

According to the obtained results, the introduction of oxygenated functionalities over the carbonaceous surface has the dual role of: (i) improving the affinity of carbon with $Mg(OH)_2$; and (ii) enhancing the hybrid material affinity with water vapour.

The oxygenated groups on the carbonaceous surface improve the dispersibility of carbon in the aqueous solution during the $Mg(OH)_2$ synthesis reaction. Hence, more carbonaceous surface is available for $Mg(OH)_2$ deposition on it. Thus, through the improvement of carbon's affinity with $Mg(OH)_2$, it was possible to deposit $Mg(OH)_2$ more compactly into the carbonaceous phase and hence to increase the density of the hybrid material (GOM and FNM samples). This allows for a higher volumetric energy density (see Figure 7c,d). The intrinsic porous nature of GO and F-CNTs permits the water vapour flowing through the bulk material from/to the deeper $Mg(OH)_2$ particles despite its compactness and hence allowing dehydration/hydration reaction.

The enhancement of the hybrid material affinity with water vapour allows for a faster rehydration kinetics (see Figure 5a,b).

It is worth to point out that the $Mg(OH)_2$ load of the hybrid materials is only ~30%. However, despite such low $Mg(OH)_2$ content, it was observed in the case of the FNM sample that a volumetric energy density increase with respect to pure $Mg(OH)_2$. GOM and pure $Mg(OH)_2$ have a comparable volumetric energy density. Nevertheless, the rehydration kinetics of GOM are superior with respect to $Mg(OH)_2$.

As a future goal, higher $Mg(OH)_2$ loads will be taken into account in order to further increase the volumetric energy density. The stability of the developed materials would be evaluated over more than 10 dehydration/hydration cycles. A study on the effect of heating rates on the heat storage step (dehydration reaction) will be considered.

5. Conclusions

In this study functionalized and un-functionalized EG/CNTs-$Mg(OH)_2$ hybrid materials have been analyzed for middle temperature thermochemical heat storage application through a laboratory-scale experimental simulation of a heat storage/release cycle.

It has been demonstrated that the carbonaceous materials improves the thermochemical performances of the storage medium in terms of hydration reaction rate and dehydration/hydration conversion with respect to pure $Mg(OH)_2$.

The hybrid materials containing functionalized EG and CNTs (GOM and FNM samples) are able to fully exploit the potential heat storage and output capacities per mass unit of $Mg(OH)_2$ (~1300 $kJ/kg_{Mg(OH)_2}$).

A higher density characterizes GOM and FNM samples. The functionalization treatment increases the compactness (and hence the density) of the hybrid materials thus allowing for higher volumetric energy density. That means, for technological application, smaller volume at equal stored/released heat. The GOM sample heat storage capacity is ~220 MJ/m^3, which is comparable to that of 100% $Mg(OH)_2$. The FNM sample exhibits an even higher heat storage capacity, about 340 MJ/m^3.

For practical uses, further development of such $C/Mg(OH)_2$ hybrid materials would need to be evaluated over more than 10 dehydration/hydration cycles. In addition, higher $Mg(OH)_2$ loads will be taken into account in order to further increase their volumetric energy density.

Acknowledgments: This study was conducted as part of the project "Development of Hybrid Materials for Energy Storage" sponsored by INSTM (Consorzio Interuniversitario Nazionale per la Scienza e Tecnologia dei Materiali). The authors would like to thank the Tokyo Institute of Technology for the provided collaboration. Financial support for covering the costs to publish in open access by INSTM is acknowledged.

Author Contributions: C. Milone, L. Bonaccorsi and Y. Kato conceived and designed the research activity and contributed reagents, materials and analysis tools; E. Mastronardo and E. Piperopoulos performed experiments and analysis. E. Mastronardo and C. Milone wrote this paper. All authors contributed equally by analyzing data and revising this paper.

Conflicts of Interest: The authors declare no conflict of interest.

Nomenclature

EG	Exfoliated graphite
CNTs	Carbon nanotubes
GO	Graphene oxide
F-CNTs	Functionalized carbon nanotubes
m_{in}	Initial sample mass (g)
m_{ist}	Instantaneous mass (g)
$M_{Mg(OH)_2}$	Molecular weight of $Mg(OH)_2$ ($g \cdot mol^{-1}$)
M_{MgO}	Molecular weight of MgO ($g \cdot mol^{-1}$)
$Q^M_{s/r}$	Heat storage and output capacities per mass unit of $Mg(OH)_2$ ($kJ \cdot kg_{Mg(OH)_2}{}^{-1}$)
$Q^V_{s/r}$	Heat storage and output capacities per volume unit ($MJ \cdot m^{-3}$)
T_d	Dehydration temperature (°C)
T_h	Hydration temperature (°C)
t	Reaction time (min)
T_{peak}	Temperatures of the derivative reacted fraction maximum peak (°C)

Greek Symbols

ϱ	Density ($kg \cdot m^{-3}$)
β	Reacted fraction (%)
$d\beta/dt$	The reaction conversion rate
β^{f}_{d}	Reacted fraction at the end of the dehydration treatment (%)
β^{i}_{d}	Reacted fraction at the beginning of the dehydration treatment (%)
β_h	Final reacted fraction of MgO at the point of water supply termination (%)
Δm_{real}	Instantaneous real mass change (%)
Δm_{th}	Theoretical mass change due to the dehydration of $Mg(OH)_2$ normalized to the total amount present in the sample (%)
$\Delta\beta_d$	Dehydration conversion (%)
$\Delta\beta_h$	Hydration conversion (%)
ΔH^0	Standard reaction enthalpy (kJ/mol)

Appendix A

Appendix A.1

The TG and the DTG profiles under inert atmosphere (Ar 100 mL/min) of GO and F-CNTs are shown in Figure A1a,b. The recorder weight loss can be associated to the CO, CO_2 and H_2O loss due to the decomposition of oxygenated groups present on carbon surface. In particular, in the GO weight loss curve two decomposition steps can be evidenced. The first consists in a rapid weight loss of ~30% at 200 °C that is indicative of the exfoliation phase typical of GO [28] provoked by the rapid release of the gases (CO, CO_2 and H_2O) generated by the decomposition of oxygenated groups present on carbon surface. The second is a slow weight loss above 300 °C. The derivative weight loss curve of GO exhibits only one peak, which corresponds to the exfoliation phase. In case of F-CNTs, several decomposition steps are observed corresponding to the de-oxygenation of the different types of functional groups attached on the carbon surface.

In both carbonaceous species, above the dehydration temperature (T_d = 350 °C), the de-oxygenation proceeds. It means that some oxygenated functionalities remain attached to the carbonaceous surface and can be responsible of the water physisorption during the rehydration step.

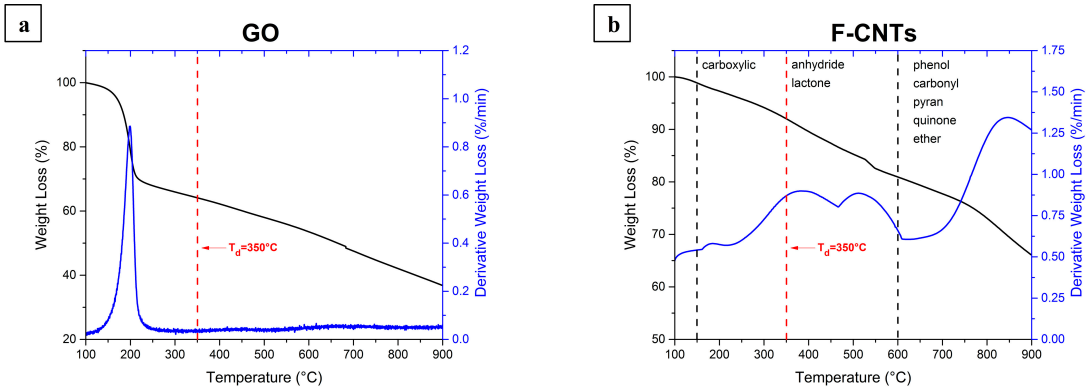

Figure A1. Weight loss and derivative weight loss of (a) GO and (b) F-CNTs.

Appendix A.2

The morphology of the carbonaceous materials used for the preparation of the hybrid materials have been analysed by means of SEM.

The as received EG consists of numerous not well-defined graphitic sheets (Figure A2a). The harsh oxidative treatment deeply modified the morphological aspect of EG, indeed, GO consists of randomly aggregated, overlapping, smaller sheets that give to this material a more fluffy aspect (Figure A2b).

The as prepared CNTs consists of entangled long carbon filaments (Figure A2c). As a result of the oxidation treatment, F-CNTs filament entanglement increases (Figure A2d) due to the electrostatic interaction between the polar functional groups introduced on the surface.

Appendix A.3

XRD pattern of GO (Figure A3a) shows the trace of the structural changes of EG after the oxidative treatment. Indeed, the precursor (EG) has a typical peak positioned near 26°, indicating a d-spacing of 0.34 nm. In GO the most intense peak is shifted near 11° (Figure A3a), which means that the d-spacing is increased at 0.78 nm.

In the small-angle XRD diffractograms of GOM sample (Figure A3b), which is indicative of an eventual increase of the GO *d*-spacing, no peaks can be detected thus confirming that the long-range order of the layer is too poor.

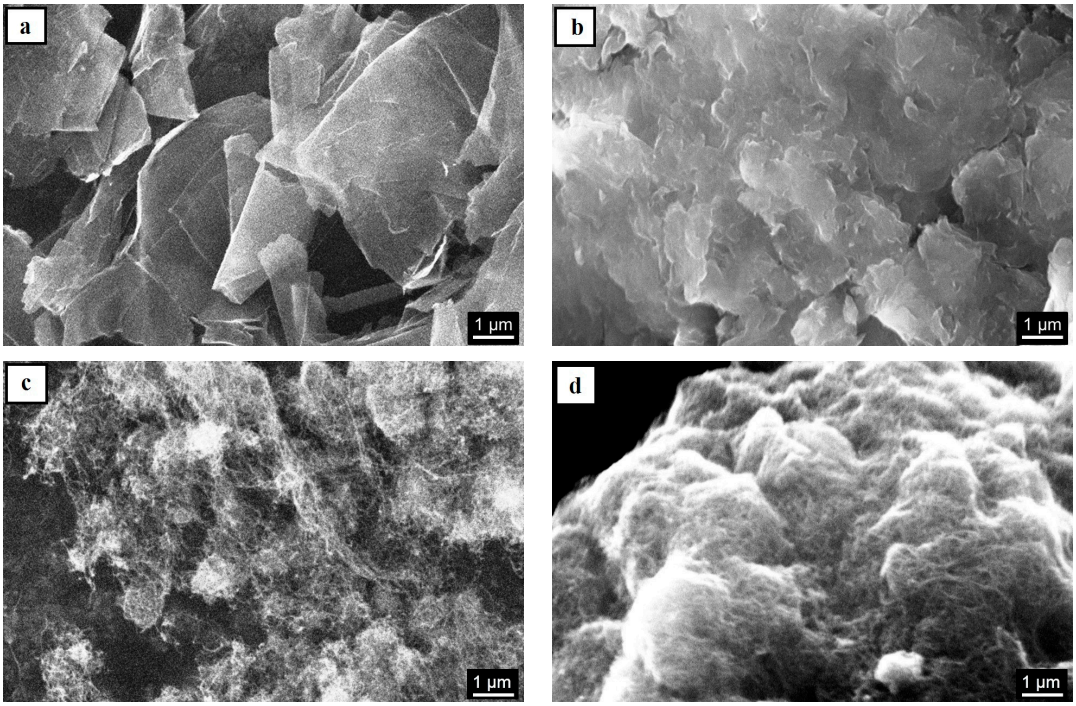

Figure A2. SEM micrographs of the carbonaceous materials: (**a**) EG; (**b**) GO; (**c**) CNTs; and (**d**) F-CNTs.

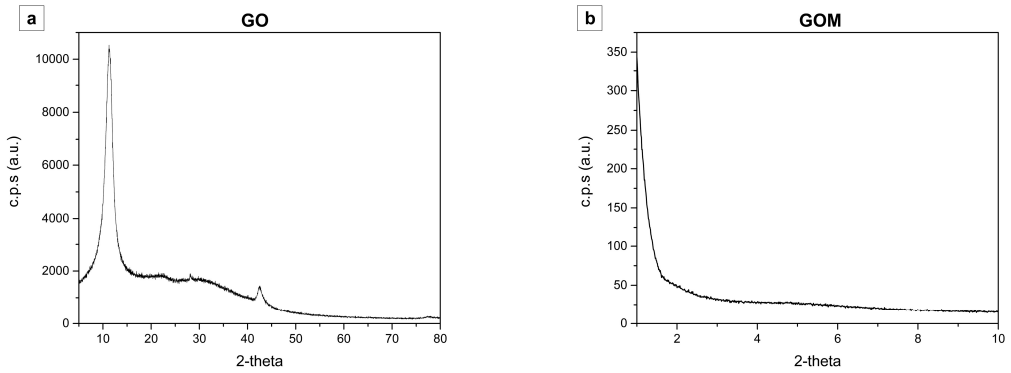

Figure A3. (**a**) XRD pattern of GO; and (**b**) small-angle XRD pattern of GOM sample.

References

1. BCS, Incorporated. *Waste Heat Recovery: Technology Opportunities in the US Industry*; U.S. Department of Energy: Washington, DC, USA, 2008; pp. 1–112.
2. Sabihuddin, S.; Kiprakis, A.E.; Mueller, M. A numerical and graphical review of energy storage technologies. *Energies* **2015**, *8*, 172–216. [CrossRef]
3. Hauer, A. *Thermal Energy Storage. Technology Brief*; IEA-ETSAP and IRENA© Technology Brief E17; International Renewable Energy Agency (IRENA): Abu Dhabi, UAE; Energy Technology Systems Analysis Programme (ETSAP): Paris, France, 2013; pp. 1–24.
4. Tomlinson, J.J. *Thermal Energy Storage Technical Progress Report*; Oak Ridge National Lab.: Oak Ridge, TN, USA, 1992; pp. 1–27.
5. Sharma, A.; Tyagi, V.V.; Chen, C.R.; Buddhi, D. Review on thermal energy storage with phase change materials and applications. *Renew. Sustain. Energy Rev.* **2009**, *13*, 318–345. [CrossRef]
6. Aydin, D.; Casey, S.P.; Riffat, S. The latest advancements on thermochemical heat storage systems. *Renew. Sustain. Energy Rev.* **2015**, *41*, 356–367. [CrossRef]

7. Pardo, P.; Deydier, A.; Anxionnaz-Minvielle, Z.; Rougé, S.; Cabassud, M.; Cognet, P. A review on high temperature thermochemical heat energy storage. *Renew. Sustain. Energy Rev.* **2014**, *32*, 591–610. [CrossRef]
8. Abedin, A.; Rosen, M. A Critical Review of Thermochemical Energy Storage Systems. *Open Renew. Energy J.* **2011**, *4*, 42–46. [CrossRef]
9. Cot-Gores, J.; Castell, A.; Cabeza, L.F. Thermochemical energy storage and conversion: A-state-of-the-art review of the experimental research under practical conditions. *Renew. Sustain. Energy Rev.* **2012**, *16*, 5207–5224. [CrossRef]
10. Kato, Y.; Harada, N.; Yoshizawa, Y. Kinetic feasibility of a chemical heat pump for heat utilization of high-temperature processes. *Appl. Therm. Eng.* **1999**, *19*, 239–254. [CrossRef]
11. Barker, R. The reactivity of calcium oxide towards carbon dioxide and its use for energy storage. *J. Appl. Chem. Biotechnol.* **2007**, *24*, 221–227. [CrossRef]
12. Yan, J.; Zhao, C.Y. Thermodynamic and kinetic study of the dehydration process of $CaO/Ca(OH)_2$ thermochemical heat storage system with Li doping. *Chem. Eng. Sci.* **2015**, *138*, 86–92. [CrossRef]
13. Felderhoff, M.; Bogdanović, B. High temperature metal hydrides as heat storage materials for solar and related applications. *Int. J. Mol. Sci.* **2009**, *10*, 325–344. [CrossRef] [PubMed]
14. Agrafiotis, C.; Roeb, M.; Schmücker, M.; Sattler, C. Exploitation of thermochemical cycles based on solid oxide redox systems for thermochemical storage of solar heat. Part 1: Testing of cobalt oxide-based powders. *Sol. Energy* **2014**, *102*, 189–211. [CrossRef]
15. Carrillo, A.J.; Sastre, D.; Serrano, D.P.; Pizarro, P.; Coronado, J.M. Revisiting the BaO_2/BaO redox cycle for solar thermochemical energy storage. *Phys. Chem. Chem. Phys.* **2016**, *18*, 8039–8048. [CrossRef] [PubMed]
16. Kato, Y.; Takahashi, F.; Watanabe, A.; Yoshizawa, Y. Thermal analysis of a magnesium oxide/water chemical heat pump for cogeneration. *Appl. Therm. Eng.* **2001**, *21*, 1067–1081. [CrossRef]
17. Shkatulov, A.; Ryu, J.; Kato, Y.; Aristov, Y. Composite material $Mg(OH)_2$/vermiculite: A promising new candidate for storage of middle temperature heat. *Energy* **2012**, *44*, 1028–1034. [CrossRef]
18. Zamengo, M.; Ryu, J.; Kato, Y. Magnesium hydroxide–Expanded graphite composite pellets for a packed bed reactor chemical heat pump. *Appl. Therm. Eng.* **2013**, *61*, 853–858. [CrossRef]
19. Mastronardo, E.; Bonaccorsi, L.; Kato, Y.; Piperopoulos, E.; Milone, C. Efficiency improvement of heat storage materials for $MgO/H_2O/Mg(OH)_2$ chemical heat pumps. *Appl. Energy* **2016**, *162*, 31–39. [CrossRef]
20. Mastronardo, E.; Bonaccorsi, L.; Kato, Y.; Piperopoulos, E.; Lanza, M.; Milone, C. Thermochemical performance of carbon nanotubes based hybrid materials for $MgO/H_2O/Mg(OH)_2$ chemical heat pumps. *Appl. Energy* **2016**, *181*, 232–243. [CrossRef]
21. Milone, C.; Piperopoulos, E.; Ansari, S.; Faggio, G.; Santangelo, S. Highly Versatile and Efficient Process for CNT Oxidation in Vapor Phase by Means of $Mg(NO_3)_2$–HNO_3–H_2O Ternary Mixture. *Fuller. Nanotub. Carbon Nanostruct.* **2015**, *23*, 1–5. [CrossRef]
22. Hummers, W.S.; Offeman, R.E. Preparation of Graphitic Oxide. *J. Am. Chem. Soc.* **1958**, *80*, 1339. [CrossRef]
23. Messina, G.; Modafferi, V.; Santangelo, S.; Tripodi, P.; Donato, M.G.; Lanza, M.; Galvagno, S.; Milone, C.; Piperopoulos, E.; Pistone, A. Large-scale production of high-quality multi-walled carbon nanotubes: Role of precursor gas and of Fe-catalyst support. *Diam. Relat. Mater.* **2008**, *17*, 1482–1488. [CrossRef]
24. Pokrovsky, O.S.; Schott, J. Experimental study of brucite dissolution and precipitation in aqueous solutions: Surface speciation and chemical affinity control. *Geochim. Cosmochim. Acta* **2004**, *68*, 31–45. [CrossRef]
25. Zhu, J.; Zhu, L.; Lu, Z.; Gu, L.; Cao, S.; Cao, X. Selectively expanding graphene oxide paper for creating multifunctional carbon materials. *J. Phys. Chem. C* **2012**, *116*, 23075–23082. [CrossRef]
26. Liu, C.; He, C.; Xie, T.; Yang, J. Reduction of Graphite Oxide Using Ammonia Solution and Detection Cr(VI) with Graphene-Modified Electrode. *Fuller. Nanotub. Carbon Nanostruct.* **2015**, *23*, 125–130. [CrossRef]
27. Compton, O.C.; Dikin, D.A.; Putz, K.W.; Brinson, L.C.; Nguyen, S.T. Electrically conductive "alkylated" graphene paper via chemical reduction of amine-functionalized graphene oxide paper. *Adv. Mater.* **2010**, *22*, 892–896. [CrossRef] [PubMed]
28. You, S.; Luzan, S.M.; Szabó, T.S.; Talyzin, A.V. Effect of synthesis method on solvation and exfoliation of graphite oxide. *Carbon* **2013**, *52*, 171–180. [CrossRef]